



# The Changing-look Blazar B2 1420+32

Hora D. Mishra<sup>1</sup> , Xinyu Dai<sup>1</sup> , Ping Chen<sup>2,3</sup> , Jigui Cheng<sup>4</sup>, T. Jayasinghe<sup>5</sup> , Michael A. Tucker<sup>6,13</sup> ,  
 Patrick J. Valley<sup>5,14</sup> , David Bersier<sup>7</sup> , Subhash Bose<sup>5,8</sup> , Aaron Do<sup>6</sup> , Subo Dong<sup>2</sup> , Thomas W.-S. Holoién<sup>9</sup> ,  
 Mark E. Huber<sup>6</sup> , Christopher S. Kochanek<sup>5,8</sup> , Enwei Liang<sup>4</sup> , Anna V. Payne<sup>6,15</sup> , Jose Prieto<sup>10</sup> , Benjamin J. Shappee<sup>6</sup> ,  
 K. Z. Stanek<sup>5,8</sup>, Saloni Bhatiani<sup>1</sup> , John Cox<sup>1</sup>, Cora DeFrancesco<sup>1</sup> , Zhiqiang Shen<sup>11</sup>, Todd A. Thompson<sup>5,8</sup> , and  
 Junfeng Wang<sup>12</sup>

<sup>1</sup> Homer L. Dodge Department of Physics and Astronomy, University of Oklahoma, Norman, OK 73019, USA; [hora.mishra@ou.edu](mailto:hora.mishra@ou.edu), [xdai@ou.edu](mailto:xdai@ou.edu)

<sup>2</sup> Kavli Institute for Astronomy and Astrophysics, Peking University, Yi He Yuan Road 5, Hai Dian District, Beijing 100871, People's Republic of China

<sup>3</sup> Department of Astronomy, School of Physics, Peking University, Yi He Yuan Road 5, Hai Dian District, Beijing 100871, People's Republic of China

<sup>4</sup> School of Physical Science and Technology, Guangxi University, Nanning 530004, People's Republic of China

<sup>5</sup> Department of Astronomy, The Ohio State University, 140 West 18th Avenue, Columbus, OH 43210, USA

<sup>6</sup> Institute for Astronomy, University of Hawai'i at Manoa, 2680 Woodlawn Drive, Honolulu, HI 96822, USA

<sup>7</sup> Astrophysics Research Institute, Liverpool John Moores University, 146 Brownlow Hill, Liverpool L3 5RF, UK

<sup>8</sup> Center for Cosmology and AstroParticle Physics, The Ohio State University, 191 West Woodruff Avenue, Columbus, OH 43210, USA

<sup>9</sup> The Observatories of the Carnegie Institution for Science, 813 Santa Barbara Street, Pasadena, CA 91101, USA

<sup>10</sup> Núcleo de Astronomía de la Facultad de Ingeniería y Ciencias, Universidad Diego Portales, Av. Ejército 441, Santiago, Chile

<sup>11</sup> Shanghai Astronomical Observatory, Chinese Academy of Sciences, 80 Nandan Road, Shanghai 200030, People's Republic of China

<sup>12</sup> Department of Astronomy, Xiamen University, Xiamen, Fujian 361005, People's Republic of China

Received 2020 November 18; revised 2021 March 15; accepted 2021 March 30; published 2021 June 7

## Abstract

Blazars are active galactic nuclei with their relativistic jets pointing toward the observer, comprising two major subclasses, flat-spectrum radio quasars (FSRQs) and BL Lac objects. We present multiwavelength photometric and spectroscopic monitoring observations of the blazar B2 1420+32, focusing on its outbursts in 2018–2020. Multiepoch spectra show that the blazar exhibited large-scale spectral variability in both its continuum and line emission, accompanied by dramatic gamma-ray and optical variability by factors of up to 40 and 15, respectively, on week to month timescales. Over the last decade, the gamma-ray and optical fluxes increased by factors of 1500 and 100, respectively. B2 1420+32 was an FSRQ with broad emission lines in 1995. Following a series of flares starting in 2018, it transitioned between BL Lac and FSRQ states multiple times, with the emergence of a strong Fe pseudocontinuum. Two spectra also contain components that can be modeled as single-temperature blackbodies of 12,000 and 5200 K. Such a collection of “changing-look” features has never been observed previously in a blazar. We measure gamma-ray–optical and interband optical lags implying emission-region separations of less than 800 and 130 gravitational radii, respectively. Since most emission-line flux variations, except the Fe continuum, are within a factor of 2–3, the transitions between FSRQ and BL Lac classifications are mainly caused by the continuum variability. The large Fe continuum flux increase suggests the occurrence of dust sublimation releasing more Fe ions in the central engine and an energy transfer from the relativistic jet to subrelativistic emission components.

*Unified Astronomy Thesaurus concepts:* Active galactic nuclei (16); Blazars (164); Radio loud quasars (1349); Black hole physics (159); Quasars (1319); Time domain astronomy (2109)

*Supporting material:* data behind figure, machine-readable tables

## 1. Introduction

Active galactic nuclei (AGNs) are subdivided into several broad categories. Type I AGNs (also called quasars or Seyfert I) show a blue continuum from an accretion disk and broad emission lines created by photoionization. The continuum flux stochastically varies with modest amplitudes (e.g., MacLeod et al. 2010) and the broad lines respond after a delay. Type II AGNs (or Seyfert II) show only narrow lines and no continuum variability (e.g., Khachikian & Weedman 1974; Nagao et al. 2001; Peterson et al. 2004). The most common paradigm to unify the two classes is to assume that the line of sight to the central engine is unobscured for Type I AGNs and obscured for Type II AGNs (e.g., Antonucci 1993; Urry & Padovani 1995). Most AGNs are not strong radio sources (i.e., “radio quiet”).

Those which are radio loud can be divided into flat- and steep-spectrum radio sources. Here, the radio emission is believed to be due to a jet. The emission from flat-spectrum radio quasars (FSRQs) is dominated by direct emission from the jet (e.g., Garofalo et al. 2018) and the steep-spectrum sources are dominated by emission from the extended “lobes,” where the jet is interacting with the ambient medium (e.g., Fanti et al. 1990). Since the jets are relativistic, emission from the jet can dominate if the jet is pointed toward the observer. In the extreme case of blazars (also optically violent variables), the jet emission dominates at all wavelengths and no emission lines from an underlying quasar are visible. Blazars also show much higher amplitude and shorter timescale variability than quasars at all wavelengths, from the radio band to  $\gamma$ -rays (e.g., Edelson & Malkan 1987; Urry & Padovani 1995; Sesar et al. 2007).

An increasingly powerful means of understanding these divisions is to discover and analyze “changing-look” AGNs, where a source moves from one class to another. Most

<sup>13</sup> DOE CSGF Fellow.

<sup>14</sup> NSF Graduate Research Fellow.

<sup>15</sup> NASA Fellow.

examples are AGNs shifting between Type I and Type II spectra (e.g., Matt et al. 2003; Bianchi et al. 2005; Marchese et al. 2012; Shappee et al. 2014), a change which calls into question the standard unification picture for the difference between these classes. With the availability of large spectroscopic and time-domain surveys, there have been a series of systematic searches that have found an increasing number of examples of such AGNs (e.g., Álvarez Crespo et al. 2016; Kollatschny et al. 2018; Ai et al. 2020). One interesting bias of these searches is that they generally exclude blazars from the search because their optical variability amplitudes are so high. This is unfortunate, because changing-look phenomena in blazars can provide a useful insight into understanding the origin and particle acceleration processes of the radio jets, the role of changing structure and geometry of the jets, and the accretion disk–jet connection (e.g., Falcke & Biermann 1995). Jets are also an important feedback mechanism at the galaxy cluster scale (e.g., McNamara & Nulsen 2012) and the galaxy scale for the milder decelerated jets in radio galaxies (Capetti et al. 2005; Ishibashi et al. 2014; Baldi et al. 2019).

Blazars can be broadly divided into two categories—FSRQs and BL Lac objects, based on the rest-frame equivalent width of the strongest broad emission line. If the equivalent width is less than 5 Å, the blazar is classified as a BL Lac object, otherwise, it is an FSRQ (Urry & Padovani 1995). An alternate classification is based on the total broad-line luminosity in units of the Eddington luminosity with the boundary at  $\sim 10^{-3} L_{\text{Edd}}$  (Ghisellini et al. 2011). As with Type I and II AGNs, there are arguments about potential unification schemes for the two classes. The broadband spectral energy distributions (SEDs) of blazars have two peaks. There is a lower-energy component from submillimeter to X-ray energies due to synchrotron emission and a high-energy component at MeV–TeV energies due to the inverse Compton process. Fossati et al. (1998) and Donato et al. (2001) proposed that FSRQs and BL Lac objects are a sequence, where the broadband SED moves blueward, with the bolometric luminosity decreasing from FSRQs to BL Lac objects because cooling is more efficient in FSRQ jets than in BL Lac objects (Ghisellini et al. 1998). In this picture, FSRQs have an efficient accretion disk powering the broad-line region (BLR) and BL Lac objects have inefficient accretion disks. Alternative unification schemes for FSRQs and BL Lac objects have been proposed (e.g., Giommi et al. 2012).

Studying systems that alternate between FSRQ and BL Lac object states, using photometric and spectroscopic data, should illuminate their differences, but there are few studies in the literature that can really be used to explore the question of blazar unification. While there are many studies of blazar variability at particular energies as well as studies of correlations of the variability between different energies and changes in the overall SED (Paliya 2015; Zhang et al. 2015; Yoo & An 2020), there are many fewer spectroscopic monitoring studies of blazars (e.g., Bregman et al. 1986; Zheng & Burbidge 1986; Perez et al. 1989; Vermeulen et al. 1995; Ulrich et al. 1997; Corbett et al. 2000). In a few cases, large emission-line flux changes have been observed. For example, Vermeulen et al. (1995) reported an increase in the H $\alpha$  luminosity by a factor of 10 for the BL Lacertae prototype VRO 42.22.01 between 1989 and 1995. More recently, Isler et al. (2013, 2015) observed broad emission line (BEL) equivalent-width changes accompanied by large Fermi  $\gamma$ -ray flares for four FSRQs.

Here we discuss observations of the blazar B2 1420+32 doing this not once, but multiple times over a two year period. B2 1420+32 at  $z = 0.682$  was identified as an FSRQ and has been detected from radio to  $\gamma$ -ray energies. From its luminosity and broad-line width, Brotherton et al. (2015) estimated a black hole mass of  $M_{\text{BH}} \simeq 4 \times 10^8 M_{\odot}$ , corresponding to a minimum light-crossing time of approximately  $r_g/c = GM_{\text{BH}}/c^3 = 0.5$  hr (rest frame). We first became interested in the source after the All-Sky Automated Survey for Supernovae (ASAS-SN; Shappee et al. 2014; Kochanek et al. 2017) detected an optical flare of  $>2$  mag on 2017 December 28 (Stanek et al. 2017) after nearly a decade of relative quiescence in the Catalina Real Time Survey (CRTS; Drake et al. 2009). At this point we started to obtain multicolor light curves using the Las Cumbres Observatory Global Telescope Network (LCOGT; Brown et al. 2013) 1 m telescopes and spectra from a variety of sources. Over the next two years, additional flares were flagged in the optical/near-IR (e.g., Carrasco et al. 2019; Marchini et al. 2019),  $\gamma$ -rays (Ciprini 2018), and even very high energy ( $E > 100$  GeV)  $\gamma$ -rays (Mirzoyan 2020).

Here we report the results of our campaign. The most striking result is that during these high-amplitude brightness fluctuations, B2 1420+32 shifted back and forth between the optical spectrum of an FSRQ and that of a BL Lac object several times, while also developing new spectral features. We discuss the photometric data in Section 2, including cross-correlation analyses between the various energy bands. We present and discuss the spectral evolution in Section 3. We consider the implications of this behavior for understanding FSRQs, blazars, and their differences in Section 4. We adopt the cosmological parameters  $\Omega_m = 0.3$ ,  $\Omega_{\Lambda} = 0.7$ , and  $H_0 = 70 \text{ km s}^{-1} \text{ Mpc}^{-1}$ .

## 2. Temporal Evolution

B2 1420+32 is detected across the entire electromagnetic spectrum—from the radio to  $\gamma$ -ray bands. In this section we examine the optical and  $\gamma$ -ray variability of B2 1420+32 and the correlations between them. We also obtained a single Swift (Gehrels et al. 2004) X-Ray Telescope (XRT; Burrows et al. 2005) X-ray observation. These results are reported in Table 1 for the optical observations and Table 2 for the  $\gamma$ -ray observations. The X-ray observation is only described in the text.

For the  $\gamma$ -rays, we analyzed the full 12 yr Fermi-LAT (Atwood et al. 2009) PASS8 data in the 0.1–500 GeV band from MJD 54689 to 59090. We used different temporal bins depending on the brightness of the source. Prior to MJD 58000, we used bins of two months, and afterwards we used bins of 3 days. During the period with LCOGT monitoring data, we used bins of a single day, and during the Transiting Exoplanet Survey Satellite (TESS) observations we used bins of 0.5 day to better match the high-cadence TESS optical data. For each bin, we performed a maximum likelihood analysis using the PYTHON script *make4FGLxml.py*<sup>16</sup> to model the source spectrum and flux. The minimum detection threshold is set at  $\text{TS} = 2.69$ , corresponding to the 90% confidence level.

The optical data came from multiple sources. The earliest data is a V-band light curve from CRTS (Drake et al. 2009). Next we used the ASAS-SN V- and g-band data (Shappee et al. 2014; Kochanek et al. 2017), with the light curves obtained

<sup>16</sup> <https://fermi.gsfc.nasa.gov/ssc/data/analysis/user/>

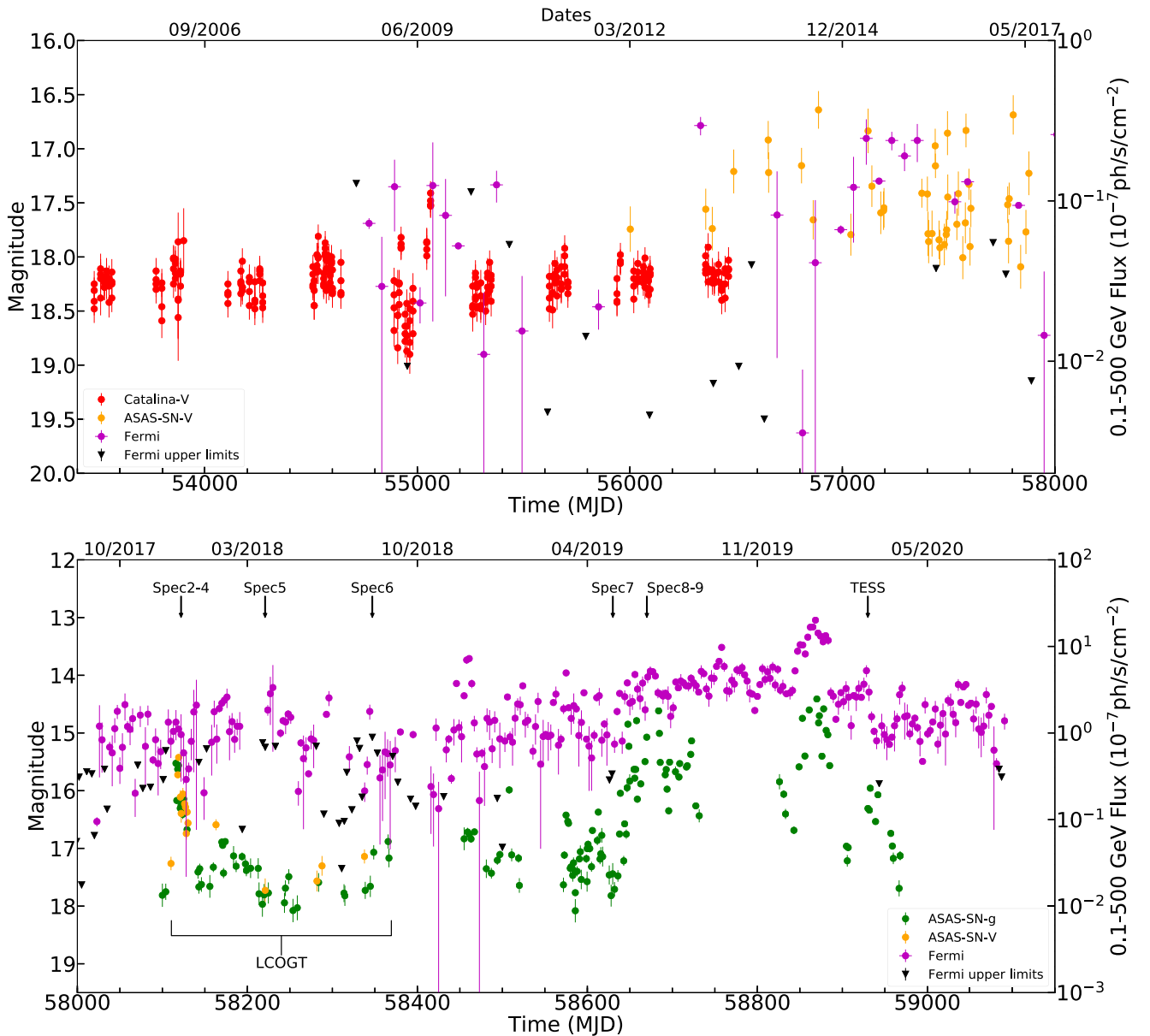


**Figure 1.** Long-term optical and 0.1–500 GeV  $\gamma$ -ray light curves of B2 1420+32, where the bottom panel shows the enhanced optical and  $\gamma$ -ray activities between MJD 58000 and 59100 and the top panel covers the range before MJD 58000. The  $\gamma$ -ray light curve is binned by 3 days in the bottom panel and 2 months in the top panel. The epochs of the spectroscopic observations, LCOGT, and TESS observations are marked.

using image subtraction as described in Jayasinghe et al. (2018) and Jayasinghe et al. (2019). B2 1420+32 was observed by TESS (Ricker et al. 2015) during Sector 23. The TESS band light curve was extracted using image subtraction methods optimized for TESS, as described in Valley et al. (2019).

We monitored B2 1420+32 in the  $B$ ,  $V$ ,  $r$  and  $i$  bands with the LCOGT (Brown et al. 2013) 1 m telescope at the McDonald Observatory. After basic reduction, the images were downloaded from Las Cumbres Observatory Science Archive (<https://archive.lco.global>). We used the IRAF (Tody 1986) `aphtot` task to perform aperture photometry with an aperture size twice the FWHM of the stellar profile. AAVSO Photometric All-Sky Survey (Henden et al. 2016) DR9 catalog stars were used for photometric calibration.

We observed B2 1420+32 with Swift (Gehrels et al. 2004) on 2018 January 20 UT 15:44:46 for 1 ks with the XRT in the WT mode. We measured a net count rate of

$0.046 \pm 0.019$  count  $s^{-1}$  in the 0.2–10 keV band with an unabsorbed flux of  $1.7 \times 10^{-12}$  erg  $cm^{-2} s^{-1}$ , assuming a power-law photon index of 1.7 and adopting a Galactic absorption of  $N_H = 1.07 \times 10^{20}$   $cm^{-2}$  (HI4PI Collaboration et al. 2016). Compared to the ROSAT All-Sky Survey flux of  $5.4 \times 10^{-13}$  erg  $cm^{-2} s^{-1}$  in the 0.1–2.4 keV band (Massaro et al. 2009) or equivalently  $9.3 \times 10^{-13}$  erg  $cm^{-2} s^{-1}$  in the 0.2–10 keV band, the X-ray flux increased by a factor of 2. Prince et al. (2019, 2021) measured an increase in X-ray activity using the Swift-XRT on MJD 58830 with an unabsorbed flux of  $8.3 \pm 1.7 \times 10^{-12}$  erg  $cm^{-2} s^{-1}$  in the 0.3–10 keV band, assuming a power-law photon index of  $1.35 \pm 0.22$ . This is a further increase in the XRT flux by a factor of 5.

Figures 1 and 2 show the optical and  $\gamma$ -ray evolution on a series of timescales. Figure 1 shows the evolution over the last 15 yr and is divided roughly into the pre- and postoutburst

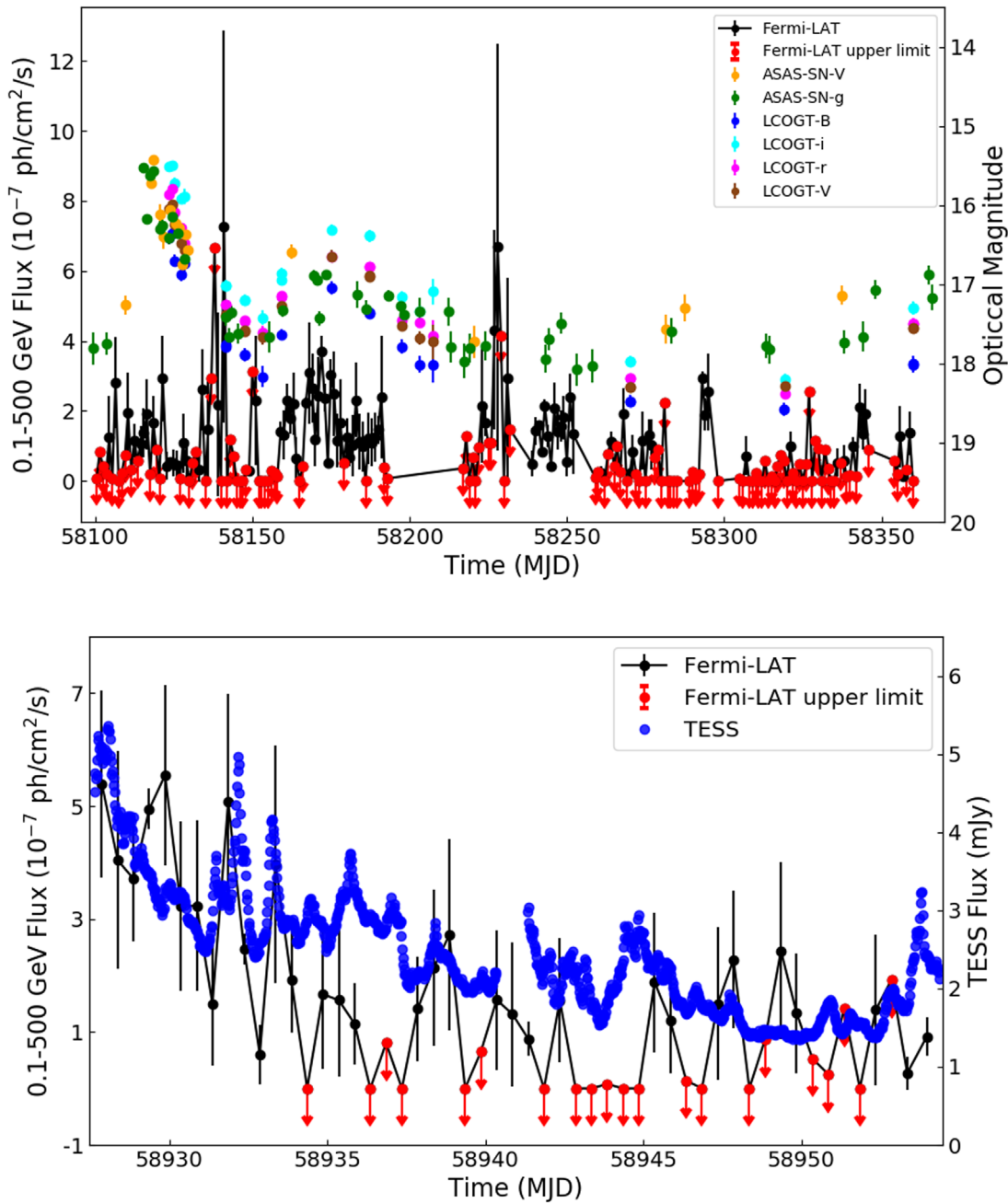


**Figure 2.** Multiband optical LCOGT, ASAS-SN, and Fermi light curves of B2 1420+32 between MJD 58124 and 58360, where the Fermi data is binned by 1 day (top). TESS and Fermi light curves of B2 1420+32 between MJD 58927 and 58954, where the TESS cadence is 30 minutes and we binned the Fermi data by 0.5 day (bottom). The optical flux shows many flares on subday timescales with amplitudes exceeding 50%.

phases. Over the entire decade-long period of photometric monitoring, the long-term  $\gamma$ -ray flux increased by a factor of 1500, when comparing the highest and lowest  $\gamma$ -ray fluxes detected, and the optical flux increased by a factor of 100. The top panel of Figure 2 shows the period in 2018 where we obtained the higher-cadence, multiband LCOGT data. Finally, the bottom panel of Figure 2 shows the 26 day period of TESS observations in early 2020. For roughly the decade prior to the ASAS-SN flare at the end of 2017, the source was fairly quiescent. The optical mean magnitude was  $\langle V \rangle = 18.3$  with a scatter of 0.20 mag. This is similar to its fluxes in the SDSS survey, measured on 2004 March 17 and the early CRTS data. Other than a weak flare in 2009 June there is little variability. Similarly, the  $\gamma$ -ray flux is low

(mean =  $1.4 \times 10^{-8}$  ph s $^{-1}$  cm $^{-2}$ ), with too few counts to really characterize the variability.

The bottom panel of Figure 1 shows that the optical flare flagged by ASAS-SN was accompanied by a  $\gamma$ -ray flare (MJD 58100–58150). The optical outburst, where the flux increases by  $3.0 \pm 0.2$  mag (factor of 16), was intensely followed-up with multiband LCOGT observations (Figure 2, top panel). However, the  $\gamma$ -ray flux does not show a significant flare at the peak of the optical outburst (MJD 58125). Afterwards, the optical flux remained somewhat higher than before the flare, but the  $\gamma$ -ray flux increases by  $2.7 \pm 0.3$  mag. Another  $\gamma$ -ray flare is observed near 2018 November (MJD 58450) when the flux increases by a factor of 16, after which the  $\gamma$ -ray flux stays in the high state, and the amplitudes of the  $\gamma$ -ray flares are

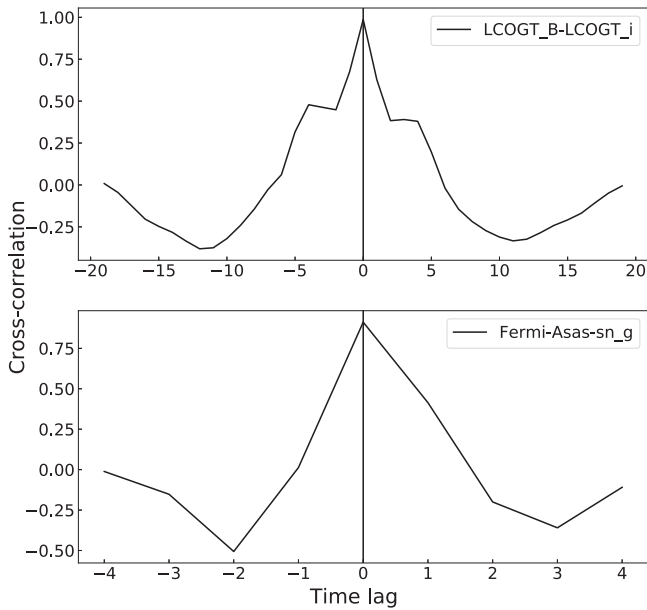


**Figure 3.** Two examples of the cross correlations between the LCOGT *B* and LCOGT *i*-band (top panel) and the Fermi and ASAS-SN *g*-band light curves’ overall peak (bottom panel) as a function of the time lag. For these cross correlations, the lag estimates are  $0.0 \pm 0.4$  day (top) and  $0.0 \pm 0.5$  day (bottom).

reduced to 1.5 mag. Then, near 2019 May, both the optical and  $\gamma$ -ray fluxes increased by another two orders of magnitude (Figure 1, bottom panel), with a further increase in 2020 March (MJD 58868) to a peak of  $g = 14.4$  mag and  $2.0 \times 10^{-6}$   $\text{ph s}^{-1} \text{cm}^{-2}$ , respectively. At this peak, the optical flux is 6 times brighter than the preflare mean, while the  $\gamma$ -ray flux is 16 times brighter. The optical and  $\gamma$ -ray data follow each other almost exactly.

Finally, the bottom panel of Figure 2 shows the brief period of TESS observations (MJD 58927–58954) with the Fermi data binned into 0.5 day intervals. The high signal-to-noise ratio (S/N) and cadence (0.5 hr) TESS light curve shows multiple, intraday flares with the flux change being as large as a factor of 4, for example, at MJD 58927 and 58933. The  $\gamma$ -ray flux appears to track the TESS light curve (Figure 2, bottom panel), although the lower S/N in the smaller temporal bins limits the comparison. While the high-amplitude  $\gamma$ -ray variability on an intraday timescale is frequently observed in blazars (e.g., Aharonian et al. 2007; Bonnoli et al. 2011; Aleksić et al. 2014), the accompanying high-amplitude (3 mag) optical variability is rare (e.g., CTA 102, D’Ammando et al. 2019).

With these overlapping optical and  $\gamma$ -ray observations and their rich, correlated temporal structures, we can look for temporal offsets between the variations at different energies. We did this using both Javelin (Zu et al. 2011) and the Interpolated Cross Correlation Function (ICCF; Peterson et al. 1998, 2004) methods, focusing on the Javelin results since they are generally less biased and provide better uncertainty estimates (Yu et al. 2020). For the interoptical bands, we used the multiband LCOGT light curves measured between MJD 58124–58360 (Figure 2, top panel), to find lags between the LCOGT *BV*, *Vr*, and *ri* light curves of  $-0.07^{+0.24}_{-0.69}$ ,  $0.05^{+0.15}_{-0.27}$ , and  $0.06^{+0.10}_{-0.43}$  days, respectively. For the  $\gamma$ -ray–optical band correlation, we first performed the analysis between the long-term Fermi and ASAS-SN *g*-band light curves between MJD

58100–59000 and around the overall peak of the light curves (MJD 58800–59000) between the Fermi and ASAS-SN *g* band, then in short periods with either significant flares or higher-quality data during the period with LCOGT coverage (MJD 58124–58360) and the TESS segment (MJD 58927–58954). The four  $\gamma$ -ray–optical lags between the long-term Fermi–ASAS-SN *g* band, Fermi–ASAS-SN *g* around the overall peak, Fermi–LCOGT *B*, and Fermi–TESS are measured as  $3.3^{+7.7}_{-6.3}$ ,  $0.9^{+0.1}_{-3.1}$ ,  $0.4^{+3.2}_{-3.6}$ , and  $-2.1^{+3.1}_{-1.5}$ , respectively. Using the ICCF method, we found that the optical light curves are well correlated with no significant interband lags, (e.g.,  $0.00 \pm 0.35$  day between *B* and *i* bands). For the  $\gamma$ -ray and the ASAS-SN light curves, we found a lag of  $0.00 \pm 0.45$  day using the ICCF method. We also confirmed that all of these light curves are significantly correlated (Figure 3). The fractional amplitudes of many of the optical and  $\gamma$ -ray flares are quite similar (Figure 1).

### 3. Spectral Evolution

We have nine spectra to examine the spectra variability, the archival SDSS spectrum from 2005 August, and eight spectroscopic follow-up observations after the 2018 January outburst. The spectra are shown in Figures 4 and 5, where we present the spectra ordered by time in Figure 4 and by absolute flux in Figure 5. The first format makes it easier to follow the evolution, while the second makes it easier to see how the spectral structure changes with luminosity. Table 3 lists the spectroscopic observations with the parameters describing the continua, and Table 4 lists the emission-line measurements. We corrected the spectra for a Galactic extinction of  $E(B - V) = 0.001$  (Schlegel et al. 1998) and converted them into the rest frame. The spectral analysis was performed using CIAO’s Sherpa software (Freeman et al. 2001), by minimizing the  $\chi^2$  statistics of the fits, which also provides uncertainties of the fitting parameters. We first fit the continuum by filtering out the spectral regions with major emission lines including Mg II, H $\beta$ , H $\gamma$ , [O III] lines, earth absorption lines, and potential artifacts from data. For spectra 1, 6, 7, 8, and 9 with significant Fe emission, we further filtered out Fe emission bands from the continuum-fitting process leaving only spectral windows with minimal Fe emission contributions. However, for spectra 8 and 9, we kept the spectral regions with moderate Fe emission contributions to increase the continuum-fitting regions and better constrain the continuum model, since the fitting process suggested more complex continuum models. For all the spectra, the continuum was fit first using a power-law model, since the nonthermal jet emission is assumed to be a power law, and we obtained reduced  $\chi^2$ /degrees of freedom of 1.8/89, 1.5/418, 2.0/4000, 1.1/1722, 0.82/4049, 2.1/3190, 1.64/1791, 1.7/546, and 1.4/348 for the nine spectra. The reduced  $\chi^2$  values are less than 2.1 for all the fits, and we generally consider them to be acceptable, because either the uncertainties of the spectra can be underestimated/overestimated or there are the still unaccounted emission-line contributions in the spectral-fitting regions. We next checked if alternative or additional model components are needed for the continuum model by examining the presence of continuous residuals above or below the best-fit models, and identified spectra 4, 7, and 8. For spectrum 4, the broken power-law model was used to improve the  $\chi^2$  value and hence the fit, where the reduced  $\chi^2$  is 0.44, significantly decreased from 1.1 for a single power law. For spectra 7 and 8, adding blackbody components have improved their fitting statistics from reduced  $\chi^2 = 1.64$  to 0.94 for spectrum 7 and

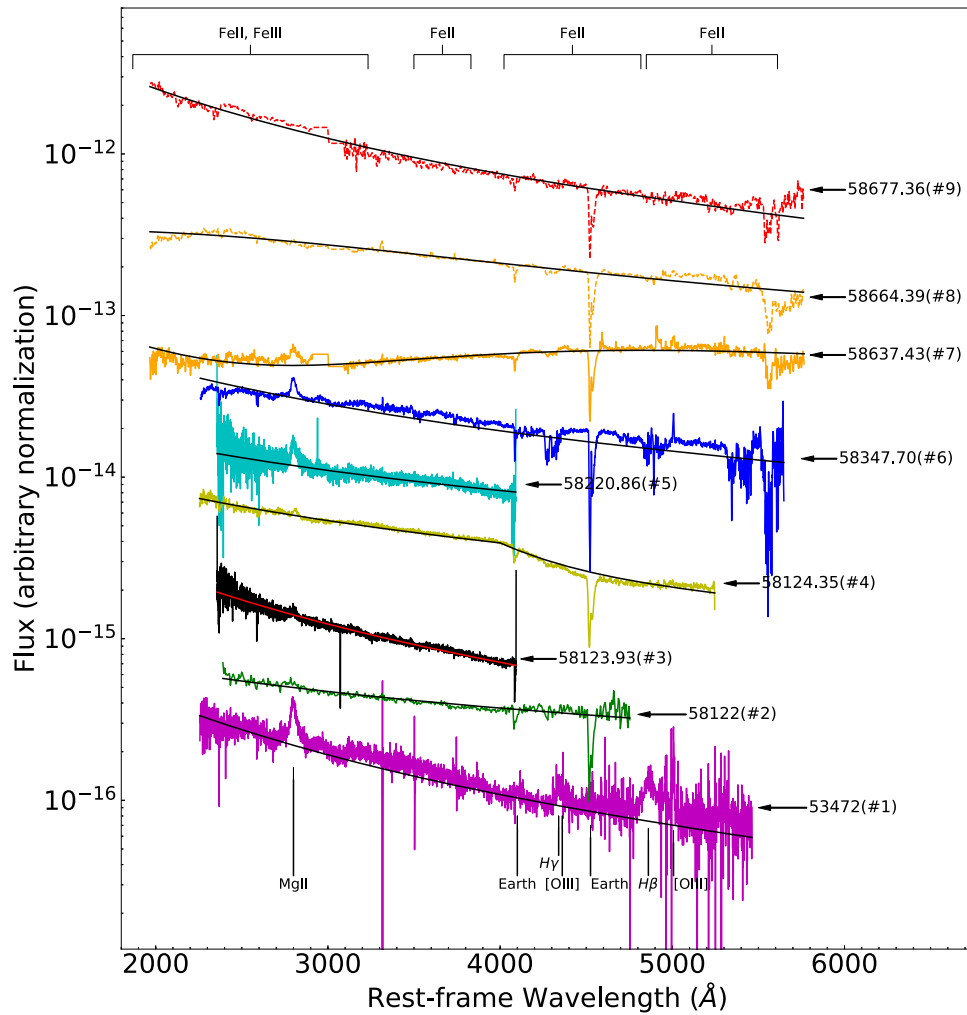


**Figure 4.** Spectroscopic evolution of B2 1420+32 in ascending chronological order from the bottom. The MJD of the observations and the spectrum number are given next to the arrows and the continuum fits are overlotted.

(The data used to create this figure are available.)

from 1.7 to 0.63 for spectrum 8. The residuals of the fittings were also more randomly scattered about the alternative broken power-law model or the addition of blackbody components for spectra 4, 7, and 8, indicating better fits compared to the single power-law model. For the emission-line measurements, we followed the general steps of Shen et al. (2011), by first fitting a local power law to the spectral regions containing the emission lines, then adding Gaussian components for the lines. We first used one Gaussian model for each emission line, and obtain reduced  $\chi^2 < 1.2$  for all the fits with the residuals randomly scattered about the best fits, suggesting single Gaussian models are adequate for modeling these lines. In most cases, we allow the line center, width, and flux to be free parameters. However, when the S/N is too low, we fix the widths of the lines to reasonable prior values. For the Fe pseudocontinuum, since the observed profiles can be quite different from those typically observed in nonjetted AGNs (Figures 4 and 5), we did not use the template-fitting method, but simply estimated the flux by subtracting the continuum from the observed spectra and excluding other known spectral lines (Tables 3 and 4).

B2 1420+32 shows rich and complex spectral changes, with multiple transitions between the FSRQ and BL Lac object

spectral types. Here we describe the main features. From spectrum 1 to 10, we see the source transition from an FSRQ (spectrum 1) → BL Lac object (spectra 2–4) → FSRQ (spectra 5–7) → BL Lac object (spectra 8–9), accompanied by complex line and continuum flux changes. Figure 6 shows the line-flux and equivalent-width variations for the nine spectral epochs. The archival SDSS spectrum (spectrum 1) of B2 1420+32 is a typical FSRQ spectrum, with a power-law continuum and broad Mg II, H $\beta$ , H $\gamma$ , and [O III] lines with equivalent widths ranging from 4 to 35 Å. Spectra 2–4 were taken during the 2018 January outburst, and we can see that the spectrum evolved into a BL Lac object spectrum with an almost featureless continuum and BEL equivalent widths  $< 5$  Å over spectra 2–4, and then back to an FSRQ in spectrum 5 when the continuum drops. The broad lines vary in both the line flux and equivalent widths. Comparing the Mg II flux and equivalent-width variations during the FSRQ → BL Lac object → FSRQ transition in spectra 1–5 (excluding spectrum 2 because of its large measurement uncertainties), we find that the Mg II flux changes by a factor of 2 and the equivalent width first decreases by a factor of 10 and then increases by a factor of 4. The much

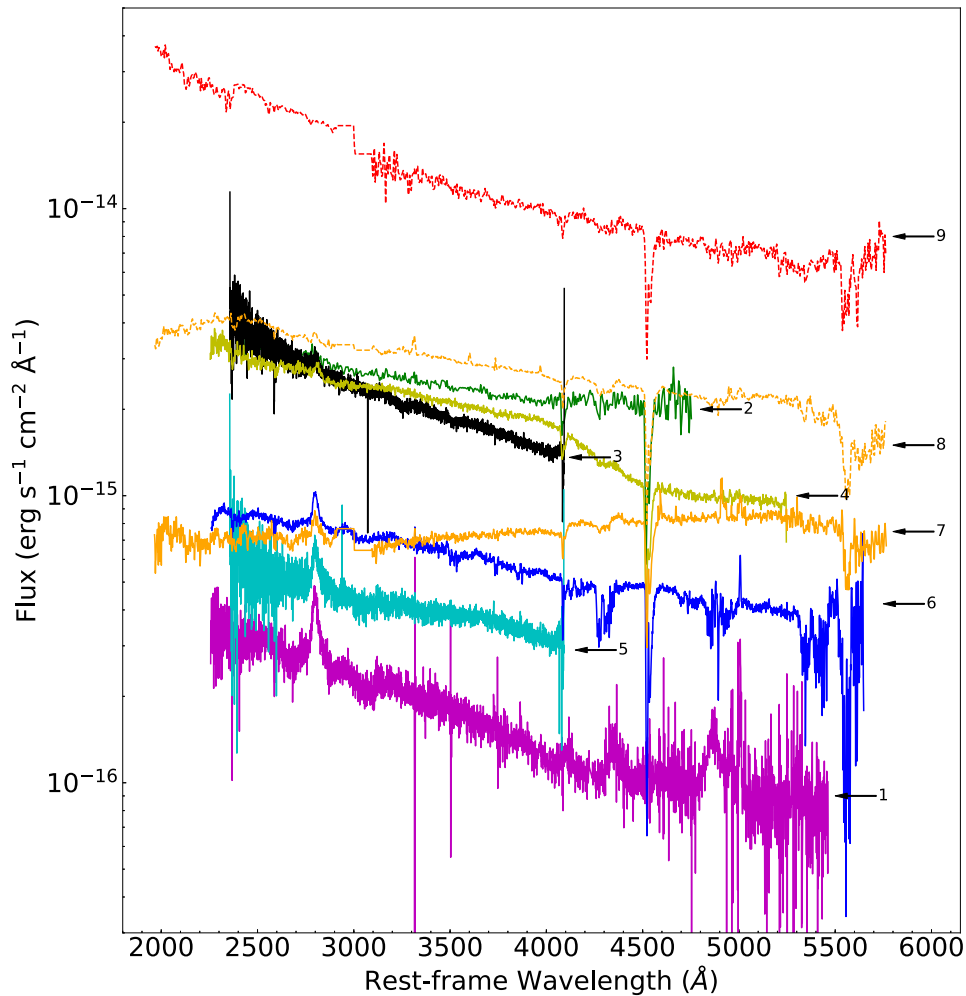


**Figure 5.** The spectra in absolute flux units. The number assigned to each spectrum describes the ascending chronological order in Table 3 and the labels in Figure 4.

larger equivalent-width variations suggest that the change to having the spectrum of a blazar is mainly due to the large changes in the continuum flux. We also correlated Mg II equivalent width with the continuum and found a negative correlation using the Pearson correlation coefficient, with a correlation coefficient of  $-0.5$ . We see a decreased Mg II equivalent width as the jet contribution increases, consistent with model predictions (e.g., Foschini 2012). Spectrum 4 exhibits a broken power-law continuum.

We continued spectroscopic monitoring as the source continued to show large  $\gamma$ -ray and optical variability. Spectrum 6 shows a significant Fe II pseudocontinuum, and spectra 7 and 8 show additional components that can be modeled with blackbodies with temperatures of 5200 and 12,000 K, respectively, on top of the power-law continuum. In spectrum 9, the continuum returned to a single power law, with the addition of Fe pseudocontinuum emission in the rest-frame ultraviolet. Between spectra 6 and 9, the source again changes from an FSRQ into a BL Lac object. The broad Mg II line flux drops by a factor of 1.7 while the equivalent width drops by a factor of 28. Figure 6 shows the evolution of emission-line fluxes and equivalent widths for the major emission lines and Fe emission. The broad H $\beta$  and H $\gamma$  lines are only marginally detected in spectra 2–8. The upper limits are best constrained in spectrum 7, where the H $\gamma$  and H $\beta$  fluxes drop by a factor of 4. The

equivalent widths drop by a factor of 9 from the SDSS spectrum. There are detections of a narrow [O III]5007 Å line in spectra 1–9. The line flux increases by a factor of 1.5 between the minimum and maximum values, while the equivalent width changes by a factor of 70. We note that while this small line-flux change could be explained by observing conditions like clouds (Fausnaugh et al. 2017), the large change in equivalent width suggests this may be a real phenomenon and not just systematics. The variations in the Mg II, H $\beta$ , H $\gamma$ , and [O III] lines are consistent with the picture that the differences between FSRQ and BL Lac object spectra are due to the changes in the continuum flux. Where they can be measured, the actual broad-line widths and fluxes change little. For example, the FWHM of Mg II is  $\sim 4000$  km s $^{-1}$  and that of [O III]5007 Å is  $\sim 500$  km s $^{-1}$ , both before and after the FSRQ  $\rightarrow$  BL Lac object  $\rightarrow$  FSRQ evolution.

#### 4. Discussion

Our multiwavelength and spectroscopic monitoring observations show that B2 1420+32 exhibits extreme spectral and temporal variability. We observe flux increases over the past two decades by factors of 1500 (8 mag) and 100 (5 mag) in the  $\gamma$ -ray and optical bands, respectively, with correlated optical and  $\gamma$ -ray variability. The  $\gamma$ -ray and optical flux changes can be up to factors of 40 and 16, respectively, on week to month

**Table 1**  
B2 1420+32 Optical Light Curves

MJD	Telescope	Band	Magnitude	Uncertainty
53479.27321	CRTS	V	18.25	0.12
53479.28138	CRTS	V	18.48	0.13
53479.28951	CRTS	V	18.31	0.12
53479.2977	CRTS	V	18.41	0.13
53562.16491	CRTS	V	18.25	0.12
53562.17136	CRTS	V	18.14	0.12
58100.00768	ASAS-SN	g	17.81	0.20
58104.00069	ASAS-SN	g	17.75	0.14
58115.98322	ASAS-SN	g	15.52	0.03
58116.97997	ASAS-SN	g	16.17	0.03
58118.02747	ASAS-SN	g	15.62	0.03
58119.02784	ASAS-SN	g	15.56	0.03
58124.0043	LCOGT	B	16.41	0.06
58125.0281	LCOGT	B	16.36	0.07
58125.9248	LCOGT	B	16.70	0.07
58128.0192	LCOGT	B	16.88	0.07
58128.9496	LCOGT	B	16.73	0.12
58141.917	LCOGT	B	17.76	0.07
58927.60	TESS		14.36	0.00
58927.62	TESS		14.35	0.00
58927.64	TESS		14.29	0.00
58927.67	TESS		14.31	0.00
58927.69	TESS		14.30	0.00
58927.71	TESS		14.25	0.00

(This table is available in its entirety in machine-readable form.)

timescales and a factor of 3 on intraday timescales in the optical. The optical and  $\gamma$ -ray light curves are well correlated with lags  $<3$  days.

We can estimate the sizes of the  $\gamma$ -ray and optical emission regions based on our variability and lag measurements. Here we use the mass reported in Brotherton et al. (2015) ( $M_{\text{BH}} \simeq 4 \times 10^8 M_{\odot}$ ), implying an Eddington luminosity of  $5.2 \times 10^{46} \text{ erg s}^{-1}$ . We also measured the black hole mass independently using  $H\beta$  line width and luminosity from the SDSS spectrum and found the mass to be consistent within 2% of the above-mentioned value, and the Mg II mass is within 40%. The black hole has a gravitational radius size of  $r_g = 5.9 \times 10^{13} \text{ cm}$ . Assuming a typical Doppler factor of  $\delta = 10$  for the jet (Hovatta et al. 2009; Liodakis et al. 2017) and considering the source redshift of  $z = 0.68$ ,  $\Delta t_{\text{intr}} = \Delta t_{\text{obs}} \delta / (1 + z)$ , an observed lag of 1 day corresponds to an emission-region size of  $260 r_g$ . The measured interoptical lags are  $<0.5$  day, corresponding to an intrinsic source size of  $<130 r_g$ . Using a conservative lag uncertainty of 3 days for our  $\gamma$ -ray–optical lag measurements on short timescales, the  $\gamma$ -ray and optical emission regions are separated by  $<800 r_g$ .

Dramatic spectral variations were also observed. In particular, we observe, for the first time, multiple rapid transitions between the FSRQ and BL Lac object spectral classifications. Few changing-look blazars have been reported previously, for example VRO 42.22.01 (Vermeulen et al. 1995) and 5BZB J0724+2621 (Álvarez Crespo et al. 2016), where a transformation from a BL Lac object to an FSRQ spectral type was observed once. For our source, the initial FSRQ spectrum with broad emission lines with Mg II,  $H\beta$ , and  $H\gamma$  evolves to the featureless spectrum of a BL Lac object, and then back again, with the reappearance of Mg II lines plus a new Fe II and Fe III pseudocontinuum and other continuum features.

**Table 2**  
B2 1420+32 Fermi-LAT Light Curves

MJD	Bin Size	Flux	Uncertainty
54772.66	2 months	0.72	0.05
54832.66	2 months	0.29	0.30
54892.66	2 months	1.22	0.58
55012.66	2 months	0.23	0.05
55072.66	2 months	1.24	1.06
55132.66	2 months	0.81	0.55
57504.0	3 days	5.57	0.48
57543.0	3 days	9.86	1.82
57567.0	3 days	7.41	5.35
57585.0	3 days	7.79	3.71
57609.0	3 days	6.06	3.70
57615.0	3 days	2.12	1.45
58104.5	1 day	12.5	11.5
58106.5	1 day	28.1	13.0
58110.5	1 day	19.5	11.3
58112.5	1 day	11.4	4.83
58114.5	1 day	10.6	4.98
58115.5	1 day	13.8	7.08
58927.86	0.5 day	53.8	16.4
58928.36	0.5 day	40.4	19.2
58928.86	0.5 day	37.1	11.0
58929.36	0.5 day	49.4	3.63
58929.86	0.5 day	55.4	15.9
58930.36	0.5 day	32.3	14.9

**Note.** The flux is in units of  $10^{-8} \text{ photon cm}^{-2} \text{ s}^{-1}$ .

(This table is available in its entirety in machine-readable form.)

However, the Balmer emission lines are never significantly detected after the first flares. The optical continuum changes in shape, where we can model it as a single power law, a broken power law, or a power law plus blackbody components, depending on the spectrum.

Our optical spectra show that the optical emission during flares is still dominated by a power-law continuum, presumably from the jet. A jet origin is particularly indicated by the broken power-law spectrum, which is a characteristic nonthermal emission feature and has never been observed from accretion disks (Gierliński et al. 2001; Wu et al. 2013).

The large change in some of the line features shows that the BLR is significantly affected by the  $\gamma$ -ray and optical flares. While the Mg II, [O III], and Balmer line fluxes vary by a factor of 2–3, the equivalent width changes can be as high as a factor of 150 because of the huge changes in the optical continuum flux. This is consistent with the less dramatic case of 3C 279, where the  $\text{Ly}\alpha$  flux is observed to vary by a factor of  $\sim 2$ , while the continuum changed by a factor of up to 50 (Koratkar et al. 1998). The lower variability amplitudes observed in these lines corroborate with the conclusions from studies of larger samples of moderate continuum variability blazars that the BLR clouds are mainly photoionized by the accretion disk with a significant contribution from the jet to the ionization (e.g., Isler et al. 2013, 2015). The relative consistency in the Mg II and [O III] line-width measurements also suggests that the BLR is only partially affected by the dramatic optical and  $\gamma$ -ray variability. The appearance of a Fe II and Fe III pseudocontinuum is the exception, where we observe a flux increase by a factor of 45 from the archival SDSS to the most recent spectrum (spectrum 9), with a peak flux of 3% of the Eddington luminosity. The nondetections of the Fe pseudocontinuum in spectra 2–5 can be

**Table 3**  
B2 1420+32 Spectra Continuum Analysis

Spectrum	Telescope	Resolution (Å)	MJD	Power-law Amplitude <sup>a</sup>	Power-law Index 1	Power-law Index 2	Blackbody $T$ (K)	Blackbody Flux <sup>b</sup>
1	SDSS	2.5	53472	$2.3^{+0.0042}_{-0.0042}$	$1.869^{+0.008}_{-0.008}$	...	...	...
2	LTLT	3	58121.5	$28^{+0.086}_{-0.086}$	$0.82^{+0.01}_{-0.01}$	...	...	...
3	2.4 m MDM	3	58123.43	$25^{+0.021}_{-0.021}$	$1.89^{+0.01}_{-0.01}$	...	...	...
4	2.16 m Xinglong	3	58123.85	$23.6^{+0.11}_{-0.11}$	$1.19^{+0.02}_{-0.02}$	$2.78^{+0.04}_{-0.04}$	...	...
5	2.4 m MDM	3	58220.36	$4.4^{+0.011}_{-0.011}$	$0.99^{+0.01}_{-0.01}$	...	...	...
6	f-JD-Palomar	7	58347.20	$7.1^{+0.033}_{-0.033}$	$1.64^{+0.01}_{-0.01}$	...	...	...
7	SNIFS	7	58637.43	$4.7^{+0.095}_{-0.097}$	$1.17^{+0.06}_{-0.06}$	...	$5200^{+29}_{-29}$	$4.8^{+0.12}_{-0.12}$
8	SNIFS	7	58664.39	$19^{+1.3}_{-1.4}$	$0.45^{+0.10}_{-0.11}$	...	$12000^{+320}_{-380}$	$6.2^{+0.35}_{-0.35}$
9	SNIFS	7	58677.36	$160^{+0.34}_{-0.34}$	$1.8^{+0.0085}_{-0.0085}$	...	...	...

**Notes.**<sup>a</sup> Normalized to 3000 Å with units of  $10^{-16}$  erg s<sup>-1</sup> cm<sup>-2</sup> Å<sup>-1</sup>.<sup>b</sup> The flux unit is  $10^{-12}$  erg s<sup>-1</sup> cm<sup>-2</sup>.

**Table 4**  
B2 1420+32 Spectra Emission-line Analysis

Spectrum	Mg II Flux <sup>a</sup>	FWHM (km s <sup>-1</sup> )	EQW <sup>b</sup> (Å)	Hβ Flux	FWHM (km s <sup>-1</sup> )	EQW (Å)	Hγ Flux	FWHM (km s <sup>-1</sup> )	EQW (Å)
(1)	(2)	(3)	(4)	(5)	(6)	(7)	(8)	(9)	(10)
1	$79^{+2.1}_{-2.1}$	$4800^{+160}_{-160}$	$34^{+0.97}_{-0.97}$	$35^{+1.8}_{-1.7}$	$3800^{+220}_{-210}$	$15^{+0.81}_{-0.77}$	$9.9^{+1.7}_{-1.6}$	$2600^{+340}_{-310}$	$4.3^{+0.75}_{-0.70}$
2	<260	<1400	$4.5^{+2.1}_{-2.1}$	...	...	...	...	...	...
3	$36^{+6.3}_{-6.3}$	3000 <sup>c</sup>	<5.9	...	...	...	...	...	...
4	$72^{+38}_{-35}$	$3200^{+2000}_{-1300}$	$3.0^{+0.81}_{-0.72}$	<21	2000 <sup>c</sup>	<0.89	<11	2000 <sup>c</sup>	<0.47
5	$58^{+6.6}_{-6.2}$	$3800^{+490}_{-430}$	$13^{+1.5}_{-1.4}$	...	...	...	...	...	...
6	$81^{+22}_{-19}$	$3600^{+1200}_{-890}$	$11^{+3.2}_{-2.7}$	...	...	...	...	...	...
7	$61^{+5.1}_{-4.9}$	$4800^{+580}_{-530}$	$13^{+1.4}_{-1.3}$	<8.0	2000 <sup>c</sup>	<1.7	$2.3^{+1.7}_{-1.7}$	2000 <sup>c</sup>	$0.49^{+0.37}_{-0.37}$
8	$48^{+14}_{-13}$	$2000^{+680}_{-550}$	$2.5^{+0.44}_{-0.45}$	...	...	...	...	...	...
9	<66	1000 <sup>c</sup>	<0.39	...	...	...	...	...	...
[O III]4363 Å Flux	FWHM (km s <sup>-1</sup> )	EQW (Å)	[O III]5007 Å Flux	FWHM (km s <sup>-1</sup> )	EQW (Å)	Fe II, Fe III 1250–3100 Å	Fe II 3530–3800 Å	Fe II 4070–4750 Å	Fe II 4900–5550 Å
(11)	(12)	(13)	(14)	(15)	(16)	(17)	(18)	(19)	(20)
$2.2^{+0.39}_{-0.39}$	480 <sup>c</sup>	$0.96^{+0.17}_{-0.17}$	$14^{+0.90}_{-0.87}$	$470^{+41}_{-38}$	$6.1^{+0.40}_{-0.39}$	...	$30^{+42}_{-42}$	...	<150
...	...	...	...	...	...	...	...	...	...
...	...	...	...	...	...	...	...	...	...
<3.3	<210	<0.15	...	...	...	...	...	...	...
...	...	...	...	...	...	...	...	...	...
<2.5	<480	<0.35	$15^{+4.2}_{-4.5}$	<420	$2.1^{+0.60}_{-0.64}$	...	<160	<110	<220
<0.67	<480	<0.16	$16^{+2.6}_{-2.4}$	$610^{+130}_{-103}$	$3.6^{+0.65}_{-0.60}$	<240	...	...	$190^{+60}_{-60}$
<2.4	<480	<0.13	$20^{+6.9}_{-6.9}$	<420	$1.1^{+0.33}_{-0.33}$	...	...	...	$770^{+52}_{-52}$
<13	<480	<0.09	<15	<420	<0.089	$5900^{+220}_{-220}$	...	...	$2300^{+87}_{-87}$

**Notes.**<sup>a</sup> Flux unit is  $10^{-16}$  erg s<sup>-1</sup> cm<sup>-2</sup>.<sup>b</sup> Equivalent width.<sup>c</sup> These parameters were fixed.

caused by the reduction of the equivalent widths by the increase of the continuum flux. The appearance of a strong Fe II and Fe III pseudocontinuum suggests the disruption of dust clouds by shocks or radiation, which would free up a large amount of Fe (e.g., Kishimoto et al. 2011; Baskin & Laor 2018; He et al. 2021). The variability in the emission-line fluxes of different species (typically a factor of 2) and Fe II and Fe III (~45) suggests energy transfers from the relativistic jet to subrelativistic components. It is also possible that the variations

in the continuum flux from the disk (e.g., Kelly et al. 2009; MacLeod et al. 2010) could drive dust destruction while being masked by the far larger variations in the jet component.

One optical spectrum (spectrum 7) shows a prominent continuum feature, which is well fitted by a 5200 K blackbody, and a second spectrum (spectrum 8) shows a prominent component well fitted by a 12,000 K blackbody. The two components have luminosities of 18%–24%  $L_{\text{Edd}}$ . The narrowness of the blackbody peaks suggests that the emission

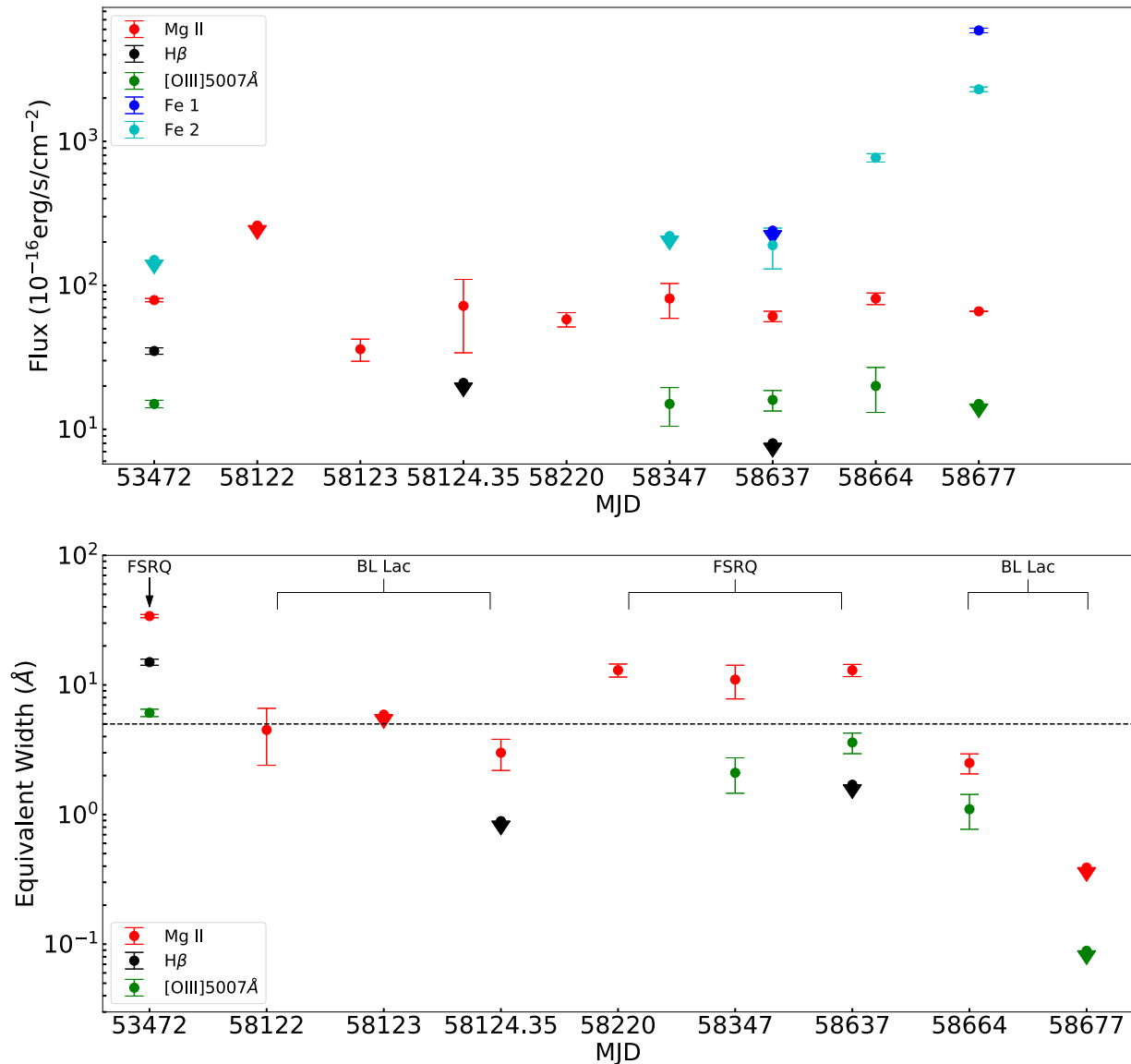


**Figure 6.** The evolution of Mg II, H $\beta$ , [O III]5007 Å, and Fe continuum fluxes from spectrum 1 to 9 in the upper panel. Fe 1 corresponds to the Fe II and Fe III emissions in 1250–3100 Å and Fe 2 corresponds to the 4900–5550 Å Fe II emission. The lower panel shows the evolution of the equivalent widths (see Table 4). The black dashed line at 5 Å denotes the equivalent-width classification between FSRQ and BL Lac object states. The downward triangles in both panels are upper limits.

source is most likely (mildly) subrelativistic, because relativistic Doppler effects will broaden any narrow features. A modification from the power-law jet emission combined with the beaming effect can mimic a single blackbody spectral shape. These single-temperature blackbody components are difficult to interpret as radiation from the accretion disk, because accretion disks span broad temperature ranges, leading to UV/optical SEDs that are essentially power laws. Blackbody-like spectral components have been observed in blazars and they are commonly interpreted as the host galaxy contribution, particularly since many of them show absorption features typical of host galaxies (e.g., Paiano et al. 2020). However, the blackbody components detected in B2 1420+32 are clearly not from the host because the host contribution is constant. Here, the blackbody components are detected only when the source is near peak brightness, while there is no significant host component visible even in the archival, low-state, SDSS spectrum.

The unique blackbody components could be from the jet itself, if the jet is precessing and we are occasionally observing a part of the jet with low Doppler-beaming factors. This model of changing viewing angles was also proposed to interpret the huge  $\gamma$ -ray and optical flux changes in CTA 102 (D’Ammando et al. 2019). Alternatively, it is possible that there are changes in the opening angles of the jet, and the blackbody component can be from episodes of jet activity with larger opening angles and low Lorentz factors propagating through a dust-rich region (presumably the torus) to free up the ions producing the Fe pseudocontinuum. Regardless of the interpretation, the low Doppler factor suggests that these narrow blackbody spectra are more representative of the jet spectrum seen at a typical location in the central engine, and not directly along the jet.

AGN feedback has been broadly classified into the “quasar mode” and “radio mode.” The “quasar mode” is feedback from either the radiation (high-Eddington regime) or disk winds in the non-Eddington regime, while the “radio mode” is kinetic feedback from decelerated radio jet/lobes in low-luminosity

radio galaxies or galaxy clusters. Strongly relativistic jets are seldom considered as important galaxy-scale feedback sources, because they penetrate through the galaxy and are only decelerated to mildly relativistic speeds for larger (cluster) scales. Here, we show that these jets may drive intermittent (mildly) subrelativistic shocks in the central engine/host galaxy with luminosities of 20%  $L_{\text{Edd}}$  or Fe emission-flux changes of 5%  $L_{\text{Edd}}$ .

Finally, we summarize the main conclusions of this paper:

1. Between 2016 and 2019, the  $\gamma$ -ray and optical fluxes increased by factors of 1500 (8 mag) and 40 (4 mag) respectively. The optical variability amplitude observed is unprecedented, with the optical flux increasing by a factor of 100 (5 mag) compared to the SDSS observations in 1995.
2. The optical- $\gamma$ -ray and interoptical band correlations constrain the  $\gamma$ -ray-optical lag to be  $<3$  days and interoptical band lags to be  $<0.5$  day, corresponding to emission distance/sizes of less than  $\sim 800 r_g$  and  $\sim 130 r_g$ .
3. B2 1420+32 is a changing-look blazar, transiting between the two major classifications of blazars, the FSRQ and BL Lac object categories, due to dramatic changes in the jet continuum flux diluting the line features.
4. Complex spectral evolution is observed in both the continuum and emission lines, suggesting dramatic changes in the jet and photoionization properties of the emission-line regions. The emergence of strong Fe II and Fe III pseudocontinua is consistent with the sublimation of dust grains by either radiation or shocks releasing more Fe ions into the broad-line regions. The Fe line fluxes approach 3%  $L_{\text{Edd}}$ .
5. For the first time, we detect components in the optical spectra consistent with single-temperature blackbody emission, with 20% of the Eddington luminosity.

This extreme variability we describe here has not been observed before. However, it may not be uncommon, because dedicated multiband and spectroscopic monitoring of blazars are still rare. Dedicated searches for more changing-look blazars will extend the changing-look AGN studies to jetted AGNs and allow us to utilize the dramatic spectral changes to reveal AGN/jet physics.

We are grateful to the referee for the helpful comments and recommendations to make the paper stronger. We thank B. Peterson, R. Pogge, and J. Zhang for helpful discussions. H.D.M. and X.D. acknowledge the financial support from the NASA ADAP program NNX17AF26G. We thank the Las Cumbres Observatory and its staff for its continuing support of the ASAS-SN project. ASAS-SN is supported by the Gordon and Betty Moore Foundation through grant GBMF5490 to the Ohio State University, and NSF grants AST-1515927 and AST-1908570. Development of ASAS-SN has been supported by NSF grant AST-0908816, the Mount Cuba Astronomical Foundation, the Center for Cosmology and AstroParticle Physics at the Ohio State University, the Chinese Academy of Sciences South America Center for Astronomy (CAS-SACA), and the Villum Foundation. B.J.S., C.S.K., and K.Z.S. are supported by NSF grant AST-1907570. B.J.S. is also supported by NASA grant 80NSSC19K1717 and NSF grants

AST-1920392 and AST-1911074. C.S.K. and K.Z.S. are supported by NSF grant AST-181440. K.A.A. is supported by the Danish National Research Foundation (DNRF132). M.A.T. acknowledges support from the DOE CSGF through grant DE-SC0019323. Support for J.L.P. is provided in part by FONDECYT through the grant 1151445 and by the Ministry of Economy, Development, and Tourism's Millennium Science Initiative through grant IC120009, awarded to The Millennium Institute of Astrophysics (MAS). T.A.T. is supported in part by a Scialog Scholar grant 24215 from the Research Corporation. We acknowledge the Telescope Access Program (TAP) funded by NAOC, CAS, and the Special Fund for Astronomy from the Ministry of Finance. P.J.V. is supported by the National Science Foundation Graduate Research Fellowship Program Under grant No. DGE-1343012.

*Facilities:* ASAS-SN, Fermi, TESS, LCOGT, LTLT, MDM Hiltner, BAO 2.16 m, Palomar, Hawaii 88in, Swift, SDSS.

### ORCID iDs

Hora D. Mishra  <https://orcid.org/0000-0002-6821-5927>  
 Xinyu Dai  <https://orcid.org/0000-0001-9203-2808>  
 Ping Chen  <https://orcid.org/0000-0003-0853-6427>  
 T. Jayasinghe  <https://orcid.org/0000-0002-6244-477X>  
 Michael A. Tucker  <https://orcid.org/0000-0002-2471-8442>  
 Patrick J. Valley  <https://orcid.org/0000-0001-5661-7155>  
 David Bersier  <https://orcid.org/0000-0001-7485-3020>  
 Subhash Bose  <https://orcid.org/0000-0003-3529-3854>  
 Aaron Do  <https://orcid.org/0000-0003-3429-7845>  
 Subo Dong  <https://orcid.org/0000-0002-1027-0990>  
 Thomas W.-S. Holoien  <https://orcid.org/0000-0001-9206-3460>  
 Mark E. Huber  <https://orcid.org/0000-0003-1059-9603>  
 Christopher S. Kochanek  <https://orcid.org/0000-0001-6017-2961>  
 Enwei Liang  <https://orcid.org/0000-0002-7044-733X>  
 Anna V. Payne  <https://orcid.org/0000-0003-3490-3243>  
 Jose Prieto  <https://orcid.org/0000-0003-0943-0026>  
 Benjamin J. Shappee  <https://orcid.org/0000-0003-4631-1149>  
 Saloni Bhatiani  <https://orcid.org/0000-0002-9044-9383>  
 Cora DeFrancesco  <https://orcid.org/0000-0002-1650-7936>  
 Todd A. Thompson  <https://orcid.org/0000-0003-2377-9574>  
 Junfeng Wang  <https://orcid.org/0000-0003-4874-0369>

### References

- Aharonian, F., Akhperjanian, A. G., Bazer-Bachi, A. R., et al. 2007, *ApJL*, 664, L71  
 Ai, Y., Dou, L., Yang, C., et al. 2020, *ApJL*, 890, L29  
 Aleksić, J., Ansoldi, S., Antonelli, L. A., et al. 2014, *Sci*, 346, 1080  
 Álvarez Crespo, N., Masetti, N., Ricci, F., et al. 2016, *AJ*, 151, 32  
 Antonucci, R. 1993, *ARA&A*, 31, 473  
 Atwood, W. B., Abdo, A. A., Ackermann, M., et al. 2009, *ApJ*, 697, 1071  
 Baldi, R. D., Rodríguez Zaurín, J., Chiaberge, M., et al. 2019, *ApJ*, 870, 53  
 Baskin, A., & Laor, A. 2018, *MNRAS*, 474, 1970  
 Bianchi, S., Guainazzi, M., Matt, G., et al. 2005, *A&A*, 442, 185  
 Bonnoli, G., Ghisellini, G., Foschini, L., et al. 2011, *MNRAS*, 410, 368  
 Bregman, J. N., Glassgold, A. E., Huggins, P. J., et al. 1986, *ApJ*, 301, 698  
 Brotherton, M. S., Singh, V., & Runnoe, J. 2015, *MNRAS*, 454, 3864  
 Brown, T. M., Baliber, N., Bianco, F. B., et al. 2013, *PASP*, 125, 1031  
 Burrows, D. N., Hill, J. E., Nousek, J. A., et al. 2005, *SSRv*, 120, 165  
 Capetti, A., Verdoes Kleijn, G., & Chiaberge, M. 2005, *A&A*, 439, 935  
 Carrasco, L., Escobedo, G., Recillas, E., et al. 2019, *ATel*, 13028, 1  
 Ciprini, S. 2018, *ATel*, 12277, 1  
 Corbett, E. A., Robinson, A., Axon, D. J., et al. 2000, *MNRAS*, 319, 685  
 D'Ammando, F., Raiteri, C. M., Villata, M., et al. 2019, *MNRAS*, 490, 5300  
 Donato, D., Ghisellini, G., Tagliaferri, G., et al. 2001, *A&A*, 375, 739

- Drake, A. J., Djorgovski, S. G., Mahabal, A., et al. 2009, *ApJ*, 696, 870
- Edelson, R. A., & Malkan, M. A. 1987, *ApJ*, 323, 516
- Falcke, H., & Biermann, P. L. 1995, *A&A*, 293, 665
- Fanti, R., Fanti, C., Schilizzi, R. T., et al. 1990, *A&A*, 231, 333
- Fausnaugh, M. M., Grier, C. J., Bentz, M. C., et al. 2017, *ApJ*, 840, 97
- Foschini, L. 2012, *RAA*, 12, 359
- Fossati, G., Maraschi, L., Celotti, A., et al. 1998, *MNRAS*, 299, 433
- Freeman, P., Doe, S., & Siemiginowska, A. 2001, *Proc. SPIE*, 4477, 76
- Garofalo, D., Singh, C. B., & Zack, A. 2018, *NatSR*, 8, 15097
- Gehrels, N., Chincarini, G., Giommi, P., et al. 2004, *ApJ*, 611, 1005
- Ghisellini, G., Celotti, A., Fossati, G., et al. 1998, *MNRAS*, 301, 451
- Ghisellini, G., Tavecchio, F., Foschini, L., et al. 2011, *MNRAS*, 414, 2674
- Gierliński, M., Maciołek-Niedźwiecki, A., & Ebisawa, K. 2001, *MNRAS*, 325, 1253
- Giommi, P., Padovani, P., Polenta, G., et al. 2012, *MNRAS*, 420, 2899
- He, Z., Jiang, N., Wang, T., et al. 2021, *ApJL*, 907, L29
- Henden, A. A., Templeton, M., Terrell, D., et al. 2016, *yCat*, II/336
- HI4PI Collaboration, Bekhti, B., Flöer, N., et al. 2016, *A&A*, 594, A116
- Hovatta, T., Valtaoja, E., Tornikoski, M., et al. 2009, *A&A*, 494, 527
- Ishibashi, W., Auger, M. W., Zhang, D., et al. 2014, *MNRAS*, 443, 1339
- Isler, J. C., Urry, C. M., Bailyn, C., et al. 2015, *ApJ*, 804, 7
- Isler, J. C., Urry, C. M., Coppi, P., et al. 2013, *ApJ*, 779, 100
- Jayasinghe, T., Kochanek, C. S., Stanek, K. Z., et al. 2018, *MNRAS*, 477, 3145
- Jayasinghe, T., Stanek, K. Z., Kochanek, C. S., et al. 2019, *MNRAS*, 485, 961
- Kelly, B. C., Bechtold, J., & Siemiginowska, A. 2009, *ApJ*, 698, 895
- Khachikian, E. Y., & Weedman, D. W. 1974, *ApJ*, 192, 581
- Kishimoto, M., Hönig, S. F., Antonucci, R., et al. 2011, *A&A*, 527, A121
- Kochanek, C. S., Shappee, B. J., Stanek, K. Z., et al. 2017, *PASP*, 129, 104502
- Kollatschny, W., Ochmann, M. W., Zetzl, M., et al. 2018, *A&A*, 619, A168
- Koratkar, A., Pian, E., Urry, C. M., et al. 1998, *ApJ*, 492, 173
- Liதாகის, I., Marchili, N., Angelakis, E., et al. 2017, *MNRAS*, 466, 4625
- MacLeod, C. L., Ivezić, Ž., Kochanek, C. S., et al. 2010, *ApJ*, 721, 1014
- Marchese, E., Braitto, V., Della Ceca, R., et al. 2012, *MNRAS*, 421, 1803
- Marchini, A., Bonnoli, G., Bellizzi, L., et al. 2019, *ATel*, 12886, 1
- Massaro, E., Giommi, P., Leto, C., et al. 2009, *A&A*, 495, 691
- Matt, G., Guainazzi, M., & Maiolino, R. 2003, *MNRAS*, 342, 422
- McNamara, B. R., & Nulsen, P. E. J. 2012, *NJPh*, 14, 055023
- Mirzoyan, R. 2020, *ATel*, 13412, 1
- Nagao, T., Murayama, T., & Taniguchi, Y. 2001, *ApJ*, 546, 744
- Paiano, S., Falomo, R., Treves, A., et al. 2020, *MNRAS*, 497, 94
- Paliya, V. S. 2015, *ApJ*, 804, 74
- Perez, E., Penston, M. V., & Moles, M. 1989, *MNRAS*, 239, 75
- Peterson, B. M., Ferrarese, L., Gilbert, K. M., et al. 2004, *ApJ*, 613, 682
- Peterson, B. M., Wanders, I., Horne, K., et al. 1998, *PASP*, 110, 660
- Prince, R., Khatoon, R., & Gupta, N. 2019, *ATel*, 13353, 1
- Prince, R., Khatoon, R., & Stalin, C. S. 2021, *MNRAS*, 502, 5245
- Ricker, G. R., Winn, J. N., Vanderspek, R., et al. 2015, *JATIS*, 1, 014003
- Schlegel, D. J., Finkbeiner, D. P., & Davis, M. 1998, *ApJ*, 500, 525
- Sesar, B., Ivezić, Ž., Lupton, R. H., et al. 2007, *AJ*, 134, 2236
- Shappee, B. J., Prieto, J. L., Grupe, D., et al. 2014, *ApJ*, 788, 48
- Shen, Y., Richards, G. T., Strauss, M. A., et al. 2011, *ApJS*, 194, 45
- Stanek, K. Z., Kochanek, C. S., Thompson, T. A., et al. 2017, *ATel*, 11110, 1
- Tody, D. 1986, *Proc. SPIE*, 627, 733
- Ulrich, M.-H., Maraschi, L., & Urry, C. M. 1997, *ARA&A*, 35, 445
- Urry, C. M., & Padovani, P. 1995, *PASP*, 107, 803
- Vallely, P. J., Fausnaugh, M., Jha, S. W., et al. 2019, *MNRAS*, 487, 2372
- Vermeulen, R. C., Ogle, P. M., Tran, H. D., et al. 1995, *ApJL*, 452, L5
- Wu, S., Lu, Y., Zhang, F., et al. 2013, *MNRAS*, 436, 3271
- Yoo, S., & An, H. 2020, *ApJ*, 902, 2
- Yu, Z., Kochanek, C. S., Peterson, B. M., et al. 2020, *MNRAS*, 491, 6045
- Zhang, B.-K., Zhou, X.-S., Zhao, X.-Y., et al. 2015, *RAA*, 15, 1784
- Zheng, W., & Burbidge, E. M. 1986, *ApJL*, 306, L67
- Zu, Y., Kochanek, C. S., & Peterson, B. M. 2011, *ApJ*, 735, 80